

Tailoring Bound State Geometry in High-Dimensional Non-Hermitian Systems

Ao Yang,^{1,2,*} Zixi Fang,^{1,2,*} Kai Zhang,^{3,†} and Chen Fang^{1,4,5,‡}

¹*Beijing National Laboratory for Condensed Matter Physics,
and Institute of Physics, Chinese Academy of Sciences, Beijing 100190, China*

²*University of Chinese Academy of Sciences, Beijing 100049, China*

³*Department of Physics, University of Michigan Ann Arbor, Ann Arbor, Michigan, 48109, United States*

⁴*Songshan Lake Materials Laboratory, Dongguan, Guangdong 523808, China*

⁵*Kavli Institute for Theoretical Sciences, Chinese Academy of Sciences, Beijing 100190, China*

It is generally believed that the non-Hermitian effect (NHSE), due to its non-reciprocal nature, creates barriers for the appearance of impurity bound states. In this paper, we find that in two and higher dimensions, the presence of geometry-dependent skin effect eliminates this barrier such that even an infinitesimal impurity potential can confine bound states in this type of non-Hermitian systems. By examining bound states around Bloch saddle points, we find that non-Hermiticity can disrupt the isotropy of bound states, resulting in concave dumbbell-shaped bound states. Our work reveals a geometry transition of bound state between concavity and convexity in high-dimensional non-Hermitian systems.

Introduction.— The non-Hermitian Hamiltonian serves as an effective tool for describing open systems that interact with environments [1–15]. Recently, non-Hermitian band systems have drawn much attention due to their intriguing phenomena that surpass the traditional Bloch band framework [16, 17]. A representative phenomenon is the non-Hermitian skin effect (NHSE) [18–42]. In one dimension, the NHSE is characterized by a large number of eigenstates localized at the ends of an open chain, well understood in the generalized Bloch band framework [20, 23, 27, 29, 35]. In two and higher dimensions, the NHSE exhibits more complexity due to the interplay between mode localization and open boundary geometries. Particularly, the NHSE may disappear under certain geometry but reappear under others. This dimensionality enriched phenomenon is referred to as the geometry-dependent skin effect (GDSE) [39, 43–50].

The topic of impurity states is fundamental in Hermitian systems and has been extensively studied due to its wide-ranging applications. For example, the Kondo effect is induced by magnetic impurities in metals [51], and Yu-Shiba-Rusinov impurity bound states appear in s-wave superconductors [52–54]. Recently, the investigation of impurity states in non-Hermitian settings, especially their interplay with NHSE, has revealed various new physical phenomena [55, 56]. A key aspect is that, NHSE creates barriers for the formation of impurity bound states due to its non-reciprocal nature [57, 58]. Consequently, a finite impurity potential is necessary to induce a bound state when NHSE is present [59]. However, these phenomena have primarily been studied in 1D non-Hermitian systems, it is still unclear whether impurity states can exhibit new properties in higher dimensions. Additionally, NHSE presents new characteristics

in higher dimensions [39, 60, 61], such as GDSE. The potential for impurity states to exhibit novel behaviors in interaction with these emerging forms of NHSE in higher dimensions remains a significant and largely unexplored research gap.

In this paper, we find that in the presence of GDSE, the impurity potential exhibits a zero threshold for the emergence of bound states, which is demonstrated by establishing an exact mapping between the bound state energy and the required impurity potential. Specifically, even an infinitesimal impurity potential can confine bound states in a non-Hermitian system exhibiting GDSE. A key reason is that the GDSE ensures the presence of Bloch saddle points, which further eliminates the barriers for the formation of impurity bound states.

In two and higher dimensions, the geometry of equal amplitude contour of wavefunction introduces a new characteristic for non-Hermitian impurity bound states. Here, we determine the geometry of bound states utilizing a mathematical tool of amoeba. We find that in two dimensions, the impurities can host anisotropic, concave bound states. This geometry feature is in sharp contrast with that observed in Hermitian systems, where bound states are typically isotropic and convex. Furthermore, we reveal a geometric transition from convexity to concavity in the bound states by manipulating the impurity potential. This transition is characterized using our method and is observable in experimental setups, such as through the local density of states patterns.

A general theory of bound states in non-Hermitian systems.— We start from a general tight-binding Hamiltonian with finite range couplings in two dimensions,

$$\begin{aligned} H_0 &= \sum_{x,y} \sum_{s,l} t_{s,l} |x,y\rangle \langle x+s,y+l| \\ &= \sum_{k_x, k_y \in \text{BZ}} \mathcal{H}_0(k_x, k_y) |k_x, k_y\rangle \langle k_x, k_y|, \end{aligned} \quad (1)$$

where $\mathcal{H}_0(k_x, k_y) = \sum_{l=-m, s=-n}^{l=M, s=N} t_{s,l} (e^{ik_x})^s (e^{ik_y})^l$, (x, y) represents the position of lattice site, and $t_{s,l}$ indicates

* These two authors contributed equally

† phykai@umich.edu

‡ cfang@iphy.ac.cn

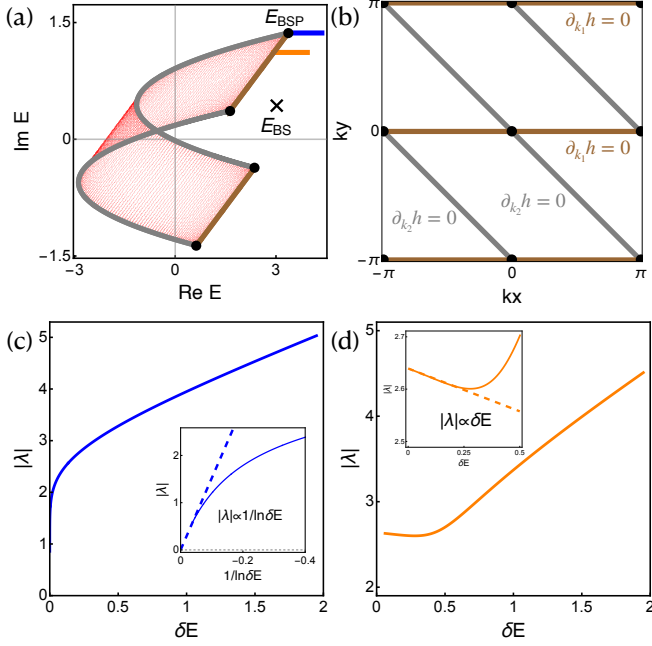


FIG. 1. (a) shows the PBC spectrum of the Hamiltonian $e^{i\pi/6} \cos(k_x + k_y) + e^{i\pi/3} \cos k_x$, with four black points denoting the energies at its BSPs. (b) illustrates the 1D Bloch saddle lines (BSLs) in the BZ, with brown lines representing $\partial_{k_y} \mathcal{H}_0(k_x, k_y) = 0$ and gray lines for $\partial_{k_x} \mathcal{H}_0(k_x, k_y) = 0$. The four intersection points, i.e., high-symmetry \mathbf{k} points in the BZ, are the BSPs and correspond to the four vertices in the spectrum shown in (a). (c) and (d) show the function $|\lambda(\delta E)|$, corresponding to the blue and orange trajectories in (a), respectively. Here, δE is defined as $E - \mathcal{H}_0(0, 0)$ in (c) and $E - \mathcal{H}_0(\pi/3, 0)$ in (d).

the hopping strength. The Bloch spectrum is formed by the eigenvalues of $\mathcal{H}_0(k_x, k_y)$ as k_x and k_y scan over the entire Brillouin zone (BZ), which we denote by σ_{PBC} [red dots in Fig. 1(a)].

To generate an impurity bound state, we place a single impurity potential of strength λ at the origin of the lattice, where the coordinate is set to $(x_0, y_0) = (0, 0)$. The impurity potential takes the form

$$V = \lambda \sum_{x,y} \delta(x,y) |x,y\rangle \langle x,y|. \quad (2)$$

One can tune the impurity strength λ such that the excited bound state has an energy E_{BS} appearing beyond the region of σ_{PBC} [the black cross in Fig. 1(a)]. Utilizing Green's function method, the wavefunction of this bound state can be analytically obtained as [62]

$$\psi_E(x, y) = \lambda \psi_E(0, 0) G_0(E; x, y), \quad (3)$$

where $G_0(E; x, y) = \langle x, y | 1/(E - H_0) | 0, 0 \rangle$ is the Green's function, H_0 is given by Eq. (1), and $\psi_E(0, 0)$ is determined by the wavefunction's normalization condition.

Setting x and y to zero in Eq. (3), the relationship between the bound state energy E_{BS} and the required impurity strength λ is established as

$$\lambda^{-1}(E_{\text{BS}}) = G_0(E_{\text{BS}}; 0, 0). \quad (4)$$

Under PBC, the Green's function on the right-hand side of Eq. (4) can be expanded under Bloch basis as an integral form, and thus the relationship becomes

$$\lambda^{-1}(E_{\text{BS}}) = \int_{\text{BZ}} \frac{dk_x dk_y}{(2\pi)^2} \frac{1}{E_{\text{BS}} - \mathcal{H}_0(k_x, k_y)}. \quad (5)$$

Typically, a state with energy within a continuum spectrum is expressed as a scattering state. Correspondingly, the energy of a bound state should lie outside the region of σ_{PBC} . The critical point, where the bound state energy merges with the PBC continuous spectrum, signifies a phase transition. This phase transition determines the minimum impurity strength required to create bound states. Consequently, we can define the set of minimum impurity strengths as

$$\Lambda = \left\{ \lim_{E_{\text{BS}} \rightarrow E_b} \lambda(E_{\text{BS}}) \mid E_b \in \partial\sigma_{\text{PBC}} \right\}, \quad (6)$$

where $\partial\sigma_{\text{PBC}}$ represents the boundary of PBC continuum spectrum, and E_b denotes a spectral boundary point. We define the impurity strength threshold λ_0 as the minimum absolute value $|\lambda|$ in the set Λ . The Bloch saddle points (BSPs), denoted as (k_x^s, k_y^s) , refer to the saddle points in the BZ where the relation holds: $\partial_{k_i} \mathcal{H}_0(k_x^s, k_y^s) = 0$ for $i = x, y$. In the following, we demonstrate that zero threshold of impurity strength is ensured by the presence of BSPs in the Bloch spectrum σ_{PBC} .

The critical response to impurity potential near BSPs.— Here, we examine the excitation around the BSP energy, which is assumed to be located at the spectrum boundary, denoted by E_b . The lattice Bloch Hamiltonian can be expanded at the BSP as $\mathcal{H}_0(q_x, q_y) = E_b + t(q_x^2 + a q_y^2 + b q_x q_y)$, where q_x and q_y are the derivations from the BSP momentum, and $\{E_b, t, a, b\}$ represent expansion coefficients. It's worth noting that the linear k_x and k_y terms have been omitted since E_b is a BSP. The $k_x k_y$ cross term can be eliminated through a proper momentum basis rotation such that certain conditions are satisfied [63]. Therefore, the expanded Hamiltonian around a BSP can be classified according to the coefficients $\{a, b\}$. For demonstration, we utilize the following concrete lattice Hamiltonian,

$$\mathcal{H}_0(k_x, k_y) = \cos k_x + a \cos k_y + b \sin k_x \sin k_y. \quad (7)$$

With a weak impurity potential, the excited bound state energy shifts slightly from the BSP energy $E_b = \mathcal{H}_0(0, 0)$, i.e., $|\delta E| = |E_{\text{BS}} - E_b| \ll 1$. Substituting Eq. (7) into Eq. (5), when $|b|, |\delta E| \ll 1$, the relationship between the impurity strength λ and the bound state energy E_{BS} becomes (see details in Supplementary Material [64]): $\lambda^{-1}(\delta E) = A(5 \ln 2 - \ln B - \ln \delta E)/2\pi$, where

the parameters $A = \sqrt{(a-2b^2)/(a^2-ab^2)}$ and $B = \sqrt{a(a+1)/(a-b^2)^2}$. Here, $\lambda^{-1}(\delta E)$ diverges asymptotically as $\ln \delta E$ when $\delta E \rightarrow 0$, which is expressed as:

$$\lambda^{-1}(\delta E) \propto \ln \delta E. \quad (8)$$

Here, we emphasize that according to the relation in Eq. (8), the excited bound state energy is highly sensitive to the impurity potential near the BSP energy, which is verified in Fig. 1(c). This stands in stark contrast to the linear response relation for excitations near the regular spectrum boundary energy, shown in Fig. 1(d). It can be expected that such response sensitivity to impurities can be utilized to detect the existence of BSPs in experiments in higher-dimensional non-Hermitian systems [46–48]. It follows from Eq. (8) that as δE approaches zero, the required impurity potential λ also tends to zero, indicating a zero threshold for the impurity potential at the BSPs. We conclude that the existence of BSPs leads to the zero threshold of impurity potential.

The numerical verification for the zero threshold at BSPs is illustrated in Fig. 1. As the bound state energy E_{BS} approaches the BSP energy E_{BSP} along the blue line in Fig. 1(a), the required impurity potential decreases to zero, as shown in Fig. 1(c). As a comparison, when E_{BS} moves toward a regular spectral boundary energy, e.g., along the orange trajectory in Fig. 1(a), the associated impurity potential approaches a finite value, as illustrated in Fig. 1(d). Dashed lines in Figs. 1(c) and (d) indicate the asymptotic behavior near the boundary.

A natural question arises: what kind of systems can ensure the existence of BSPs in higher dimensions? The answer lies in systems that exhibit GDSE. In GDSE, there are two special directions, in which the momenta are denoted by k_1 and k_2 , respectively. When boundary cuts are made along these directions, the resulting open boundary eigenstates manifest as Bloch waves. By imposing the open boundary conditions along the k_1 direction and periodic boundary conditions along the k_2 direction, k_2 momentum is conserved, allowing the Hamiltonian to be treated as a 1D k_1 -subsystem for a fixed k_2 . Since the system has no skin effect in the k_1 direction, the energy spectrum forms an arc along this direction. The endpoints of this arc satisfy $\partial_{k_1} \mathcal{H}_0(k_1, k_2) = 0$. As k_2 varies from $-\pi$ to π , these endpoints form two lines [the brown lines shown in Fig. 1(b)]. Similarly, two additional lines can be obtained for the k_2 direction [the black lines illustrated Fig. 1(b)]. At the intersections of these four lines, the BSP conditions, $\partial_{k_i} \mathcal{H}_0(k_x^s, k_y^s) = 0$ for $i = x, y$, are satisfied. Thus, these intersections correspond to four BSPs within the BZ. An illustrative example with $\{k_1, k_2\} = \{k_x, k_x + k_y\}$ is presented in Fig. 1(b), where the intersections are denoted by black dots.

Tailoring the geometry of bound states.— According to Eq. (3), the bound state wave function is determined by Green’s function. The Green’s function can be expressed in an integral form with the Hamiltonian H_0 given by

Eq. (1):

$$G_0(E_{\text{BS}}; x, y) = \oint_{\mathbb{T}^2} \frac{dz_x dz_y}{(2\pi i)^2} \frac{e^{x \ln z_x + y \ln z_y}}{z_x z_y (E - \mathcal{H}_0(z_x, z_y))}. \quad (9)$$

Here, we have extended the real momentum k to the complex value $\tilde{k}_j = k_j + i\mu_j$ and defined $z_j = e^{ik_j}$ for $j = x, y$. Under PBC, the integral contour is the BZ ($|z_x| = |z_y| = 1$), a torus in \mathbb{C}^2 space, which we denote as \mathbb{T}^2 . To compute this double integral, we adopt a step-by-step integration strategy. Firstly, we evaluate the first integral using the residue theorem. Secondly, for the second integral, as we are primarily concerned with the asymptotic behavior of the wave function far from the impurity ($|x|, |y| \gg 1$), we can use the saddle-point approximation to handle the second integral, resulting in [64]:

$$\psi_{E_{\text{BS}}}(x, y) \propto G_0(E_{\text{BS}}; x, y) \propto e^{i\tilde{\mathbf{k}}_s(\theta) \cdot \mathbf{r}}. \quad (10)$$

Here, $\mathbf{r} = (x, y)$ and the complex momentum vector $\tilde{\mathbf{k}}_s(\theta) = (\tilde{k}_{s,x}(\theta), \tilde{k}_{s,y}(\theta))$ is a saddle point of the exponent $x \ln z_x + y \ln z_y = x\tilde{k}_x + y\tilde{k}_y$ in Eq. 9, depending on the spatial direction $\theta = \arg(\mathbf{r})$. Eq. (10) demonstrates that the bound state wave function exhibits exponential behavior characterized by the complex momentum $\tilde{\mathbf{k}}$ along a fixed direction θ , resulting in anisotropy in space. Therefore, we define the characteristic localization \mathbf{l} that satisfies the relation: $|\psi_{E_{\text{BS}}}(l_x, l_y)|/|\psi_{E_{\text{BS}}}(0, 0)| = e^{-1}$, which is further expressed as:

$$\mu_x l_x + \mu_y l_y = 1. \quad (11)$$

Here, $(l_x, l_y) = l(\cos \theta, \sin \theta)$ forms a closed loop as θ changes, which characterizes the localization behavior and describes the geometric shape of impurity bound states.

For a fixed direction θ , the complex momentum $\tilde{\mathbf{k}}$ is determined by solving specific constraints (see details in the Supplementary Material [64]). The first constraint is the bulk characteristic equation,

$$f(E_{\text{BS}}, \tilde{k}_x, \tilde{k}_y) = \det[E_{\text{BS}} - \mathcal{H}_0(\tilde{k}_x, \tilde{k}_y)] = 0. \quad (12)$$

The set of imaginary parts (μ_x, μ_y) of the complex momentum $\tilde{\mathbf{k}}$ that satisfy the characteristic equation in Eq. (12) is termed amoeba, as represented by the gray regions in Figs. 2(c1) and (c2). Since $E_{\text{BS}} \notin \sigma_{\text{OBC}}$ [65], the corresponding amoeba always features a central hole [66], as shown by the blank region in Fig. 2(c1) and (c2). Moreover, by solving Eq. (12), \tilde{k}_x or \tilde{k}_y can be expressed as a function of the other. By applying the saddle point approximation $\partial_{\tilde{k}_y}(x\tilde{k}_x + y\tilde{k}_y) = 0$ to the exponential factor in Eq. (10) and utilizing the implicit function theorem $\nabla_{\tilde{\mathbf{k}}} \mathcal{H}_0 \cdot d\tilde{\mathbf{k}} = 0$, the second constraint can be derived as

$$y \partial_{\tilde{k}_x} \mathcal{H}_0 - x \partial_{\tilde{k}_y} \mathcal{H}_0 = 0. \quad (13)$$

So far, for impurity bound state, the first constraint in Eq. (12) relates the solution domain of (μ_x, μ_y) to

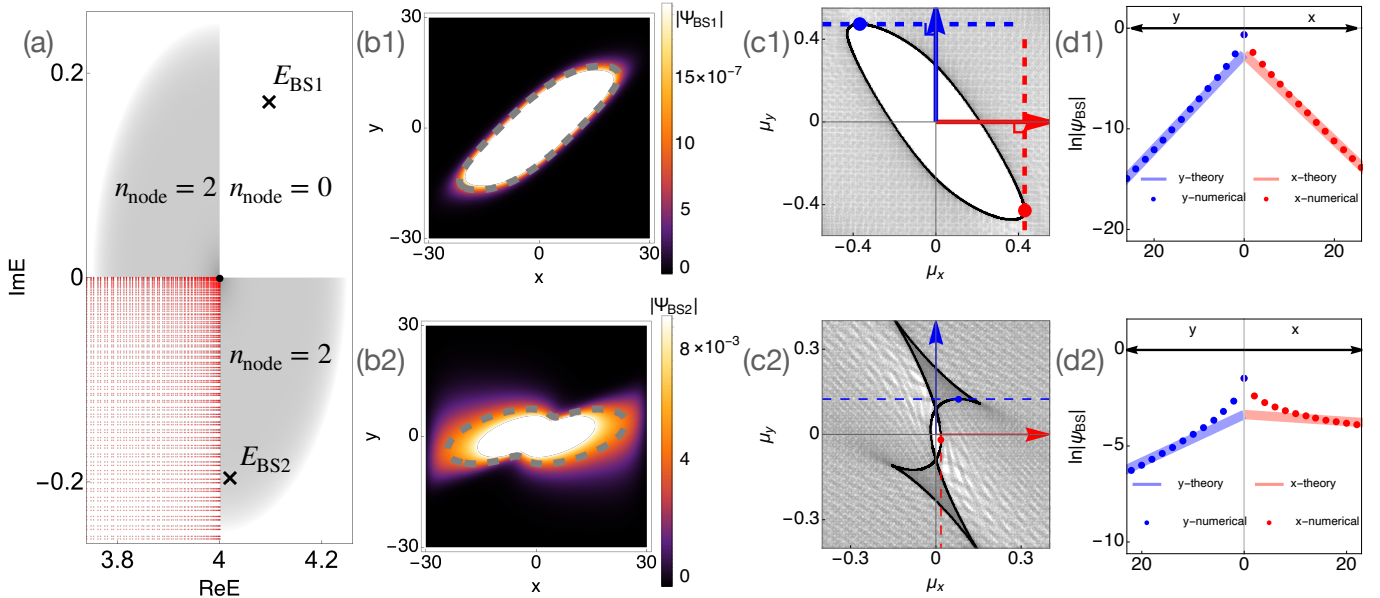


FIG. 2. Parameters $\{t_{1,1}, t_{-1,-1}, t_{1,0}, t_{-1,0}, t_{0,0}\}$ for Hamiltonian in Eq. (1) are set to be $\{2, 2, i, i, -2i\}$. (a) displays the spectrum near the Bloch saddle point $\mathcal{H}_0(0, 0)$ with $\lambda = 2.66 + 0.96i, 2.27 + 2.23i$ for the bound state E_{BS1} and E_{BS2} . (b1) and (b2) depict bound states with energy E_{BS1} and E_{BS2} , and (c1) and (c2) show the corresponding amoeba's contours outlined by the black curves. (d) Comparison of bound states between simulated data (colored dots) and theoretical data (colored line). The red (blue) dots and line in (d) correspond to the x(y)-axis. The results are obtained from simulations performed on a 30×30 lattice.

the mathematical term amoeba; the second constraint in Eq. (13), combined with Eq.(12), locates several isolated points $\mu_s(\theta)$ on amoeba. By changing the spatial direction $\theta = \arg \mathbf{r}$, $\mu_s(\theta)$ will form a closed loop which corresponds to a mathematical concept called the amoeba's contour [67–69]. As shown in Figs. 2(c1) and (c2), the amoeba's contours are represented by the black curves. The constraint given by Eq. (13) is a homogeneous function of x and y , which depends solely on the spatial direction $\theta = \arctan(y/x)$. Therefore, the bound state wavefunction exhibits exponential localization away from the impurity site, while it is not isotropic in real space. Furthermore, by applying implicit function theorem $\nabla_{\mathbf{k}} \mathcal{H}_0 \cdot d\mathbf{k} = 0$ to Eq. (13), it can be transformed into the form $\mathbf{r} \cdot d\mathbf{k} = 0$. Notably, this is a complex equation, and by taking its imaginary part, we obtain

$$\mathbf{r} \cdot d\boldsymbol{\mu} = 0. \quad (14)$$

This formula indicates that the inverse localization length $\boldsymbol{\mu}(\theta)$ of bound states along each spatial direction \mathbf{r} is determined by the value $\boldsymbol{\mu}(\theta) = (\mu_x, \mu_y)$ on the amoeba's contour, where the tangent direction is perpendicular to \mathbf{r} .

As a result, for a fixed direction \mathbf{r} , we can determine the inverse localization length $\boldsymbol{\mu}(\theta)$ using Eq. 12 and Eq. 13. By varying the spatial direction $\theta = \arg \mathbf{r}$, we find that the set of $\boldsymbol{\mu}(\theta)$ forms a closed loop on the amoeba, corresponding to the amoeba's contour. Additionally, Eq. 14

indicates that the tangent direction of $\boldsymbol{\mu}(\theta)$ is perpendicular to \mathbf{r} .

By substituting the values of (μ_x, μ_y) into Eq. (11), we can determine the geometric shape of the bound state. As illustrated in Fig. 2(a), the bound states with energies E_{BS1} and E_{BS2} are illustrated in Figs. 2(b1) and (b2), respectively. Their corresponding amoebas are calculated in Figs. 2(c1) and (c2). To further delve into the localization behaviors, we plot $\ln |\psi_{E_{BS}}(x, 0)|$ and $\ln |\psi_{E_{BS}}(0, y)|$ for these two bound states in Figs 2(d1) and (d2). According to our conclusion, the decay rate of bound states along the x and y directions are determined by the corresponding points on the amoeba's contours, which are illustrated by the red and blue dots in Figs 2(c1) and (c2). As the numerical verifications in Figs 2(d1) and (d2), the corresponding slopes at the amoeba's contour points are represented by the red and blue solid lines, matching exactly with the numerical bound state wavefunctions, as indicated by the red and blue dots.

We conclude that the amoeba's contour encodes the localization lengths of the bound state along each spatial direction. Therefore, the characteristic geometric shape of the bound state wavefunction can be tailored by the amoeba's contour. Moreover, since the amoeba's contour is determined by the bulk Hamiltonian of the system, it is expected that non-Hermitian systems can host unique bound state geometric features beyond those observed in conventional Hermitian systems.

Geometry transition of bound state under weak impu-

urity analysis.—

Here, by perturbation analysis with a weak impurity potential excitation, we demonstrate a geometry transition unique to higher-dimensional non-Hermitian systems. As previously mentioned, the non-Hermitian systems having GDSE ensure the existence of BSPs, where the bound state can be excited by an infinitesimal impurity potential. Therefore, GDSE system provides a platform to examine the bound state geometry features with a weak impurity excitation. As we established before, the bound state geometry can be tailored by the amoeba's contour. The latter is fully determined by the characterization equation $f(E_{\text{BS}}, k_x, k_y) = E_{\text{BS}} - \mathcal{H}_0(k_x, k_y)$. Here, we only consider its expansion near BSP energy E_{BSP} , which is generally expressed as:

$$f(E_{\text{BS}}, k_x, k_y) = E_{\text{BS}} - E_{\text{BSP}} - k_x^2 - e^{i\theta} k_y^2. \quad (15)$$

Here, the linear term of k_x and k_y vanishes due to the BSP condition, and cross term $k_x k_y$ is omitted for simplicity [64]. By applying the constraints in Eq. (12) and Eq. (13), we can derive an algebraic curve of order 8 that describes the amoeba's contour (see details in Supplementary Material [64]). Based on Eq. (11), we ultimately obtain an algebraic curve that features the bound state geometry shape:

$$[l_x^2 \sin \alpha + l_y^2 \sin(\alpha - \theta)]^2 - 4[l_x^2 \cos \alpha + l_y^2 \cos(\alpha - \theta)] = 4, \quad (16)$$

where $\alpha = \arg(E_{\text{BS}} - E_{\text{BSP}})$. This curve describes the localization length of the wave function along different directions and determines the shape of the bound states.

When $\theta = 0$, the Hamiltonian reduces to Hermitian, and the geometry curve collapses into a circle, given by

$$\sin^2 \alpha (l_x^2 + l_y^2)^2 - 4 \cos \alpha (l_x^2 + l_y^2) = 4. \quad (17)$$

Therefore, the shape of the bound state in Hermitian limit is always circular (or elliptical due to a scaling

factor on k_x or k_y). However, when $\theta \neq 0$, as illustrated in Fig. 2(a), varying α leads to a transition in the shape of the bound state from a regular convex curve in Fig. 2(b1) to a concave and dumbbell-like curve in Fig. 2(b2), which is unique to higher-dimensional non-Hermitian systems. This transition corresponds to the transition of the amoeba's contour from a regular curve in Fig. 2(c1) to an irregular curve with multiple singular nodes in Fig. 2(c2). Here, a curve is considered as convex if and only if it exhibits positive or negative curvature tracing along its path, while a singular node is defined as the singular point at which the curve intersects with itself. The nodes always appear in pairs due to reciprocity symmetry in GDSE systems. We show that concave geometry of bound states appears if and only if the phase $(\alpha - \theta)$ or $(\theta - \alpha)$ falls within the range of $(0, \theta)$. The proof is detailed in Supplementary Material [64]. For weak impurity excitation near BSPs, when $\theta < \alpha < 2\theta$ or $-\theta < \alpha < 0$, as indicated by the gray region in Fig. 2(a), the amoeba contour exhibits two nodes. Consequently, the geometry of the corresponding bound state wave function is concave.

Conclusion.— In summary, we investigate the characteristics of impurity-induced bound states in 2D non-Hermitian lattice systems. Our findings indicate that existence of BSPs can eliminate the threshold for the formation of impurity bound states. Notably, in a system with GDSE, even an infinitesimal impurity potential can generate bound states near the BSP energy. Such systems serve as optimal platforms for the investigation of bound states with weak excitations near BSPs. The geometry of these bound state wavefunctions is concave and anisotropic, in sharp contrast with convex, isotropic shapes observed in Hermitian systems. The existence of such bound states demonstrates that non-Hermitian properties can significantly enrich the geometric configurations of bound states.

-
- [1] Ingrid Rotter, “A non-hermitian hamilton operator and the physics of open quantum systems,” *Journal of Physics A: Mathematical and Theoretical* **42**, 153001 (2009).
- [2] Sebastian Diehl, Enrique Rico, Mikhail A. Baranov, and Peter Zoller, “Topology by dissipation in atomic quantum wires,” *Nature Physics* **7**, 971–977 (2011).
- [3] Simon Malzard, Charles Poli, and Henning Schomeerus, “Topologically protected defect states in open photonic systems with non-hermitian charge-conjugation and parity-time symmetry,” *Phys. Rev. Lett.* **115**, 200402 (2015).
- [4] Jean Dalibard, Yvan Castin, and Klaus Mølmer, “Wave-function approach to dissipative processes in quantum optics,” *Phys. Rev. Lett.* **68**, 580–583 (1992).
- [5] Alois Regensburger, Christoph Bersch, Mohammad-Ali Miri, Georgy Onishchukov, Demetrios N. Christodoulides, and Ulf Peschel, “Parity–time synthetic photonic lattices,” *Nature* **488**, 167–171 (2012).
- [6] T. Gao, E. Estrecho, K. Y. Bliokh, T. C. H. Liew, M. D. Fraser, S. Brodbeck, M. Kamp, C. Schneider, S. Höfling, Y. Yamamoto, F. Nori, Y. S. Kivshar, A. G. Truscott, R. G. Dall, and E. A. Ostrovskaya, “Observation of non-Hermitian degeneracies in a chaotic exciton-polariton billiard,” *Nature* **526**, 554–558 (2015).
- [7] Liang Feng, Ramy El-Ganainy, and Li Ge, “Non-Hermitian photonics based on parity–time symmetry,” *Nature Photonics* **11**, 752–762 (2017).
- [8] Ramy El-Ganainy, Konstantinos G. Makris, Mercedeh Khajavikhan, Ziad H. Musslimani, Stefan Rotter, and Demetrios N. Christodoulides, “Non-Hermitian physics and PT symmetry,” *Nature Physics* **14**, 11–19 (2018).
- [9] Mohammad-Ali Miri and Andrea Alù, “Exceptional points

- in optics and photonics,” *Science* **363**, eaar7709 (2019).
- [10] Ş. K. Özdemir, S. Rotter, F. Nori, and L. Yang, “Parity-time symmetry and exceptional points in photonics,” *Nature Materials* **18**, 783–798 (2019).
- [11] Vladyslav Kozii and Liang Fu, “Non-Hermitian Topological Theory of Finite-Lifetime Quasiparticles: Prediction of Bulk Fermi Arc Due to Exceptional Point,” arXiv:1708.05841 (2017).
- [12] Huitao Shen and Liang Fu, “Quantum oscillation from in-gap states and a non-hermitian landau level problem,” *Phys. Rev. Lett.* **121**, 026403 (2018).
- [13] Yuki Nagai, Yang Qi, Hiroki Isobe, Vladyslav Kozii, and Liang Fu, “DMFT Reveals the Non-Hermitian Topology and Fermi Arcs in Heavy-Fermion Systems,” *Phys. Rev. Lett.* **125**, 227204 (2020).
- [14] Fei Song, Shunyu Yao, and Zhong Wang, “Non-hermitian skin effect and chiral damping in open quantum systems,” *Phys. Rev. Lett.* **123**, 170401 (2019).
- [15] Yuto Ashida, Zongping Gong, and Masahito Ueda, “Non-hermitian physics,” *Advances in Physics* **69**, 249–435 (2020), doi: 10.1080/00018732.2021.1876991.
- [16] Huitao Shen, Bo Zhen, and Liang Fu, “Topological Band Theory for Non-Hermitian Hamiltonians,” *Phys. Rev. Lett.* **120**, 146402 (2018).
- [17] Kohei Kawabata, Ken Shiozaki, Masahito Ueda, and Masatoshi Sato, “Symmetry and Topology in Non-Hermitian Physics,” *Phys. Rev. X* **9**, 041015 (2019).
- [18] Tony E. Lee, “Anomalous edge state in a non-hermitian lattice,” *Phys. Rev. Lett.* **116**, 133903 (2016).
- [19] V. M. Martinez Alvarez, J. E. Barrios Vargas, and L. E. F. Foa Torres, “Non-hermitian robust edge states in one dimension: Anomalous localization and eigenspace condensation at exceptional points,” *Phys. Rev. B* **97**, 121401(R) (2018).
- [20] Shunyu Yao and Zhong Wang, “Edge States and Topological Invariants of Non-Hermitian Systems,” *Phys. Rev. Lett.* **121**, 086803 (2018).
- [21] Flore K. Kunst, Elisabet Edvardsson, Jan Carl Budich, and Emil J. Bergholtz, “Biorthogonal Bulk-Boundary Correspondence in Non-Hermitian Systems,” *Phys. Rev. Lett.* **121**, 026808 (2018).
- [22] Shunyu Yao, Fei Song, and Zhong Wang, “Non-Hermitian Chern Bands,” *Phys. Rev. Lett.* **121**, 136802 (2018).
- [23] Kazuki Yokomizo and Shuichi Murakami, “Non-Bloch Band Theory of Non-Hermitian Systems,” *Phys. Rev. Lett.* **123**, 066404 (2019).
- [24] Ching Hua Lee and Ronny Thomale, “Anatomy of skin modes and topology in non-Hermitian systems,” *Phys. Rev. B* **99**, 201103(R) (2019).
- [25] Ching Hua Lee, Linhu Li, and Jiangbin Gong, “Hybrid Higher-Order Skin-Topological Modes in Nonreciprocal Systems,” *Phys. Rev. Lett.* **123**, 016805 (2019).
- [26] Stefano Longhi, “Probing non-hermitian skin effect and non-bloch phase transitions,” *Phys. Rev. Res.* **1**, 023013 (2019).
- [27] Kai Zhang, Zhesen Yang, and Chen Fang, “Correspondence between Winding Numbers and Skin Modes in Non-Hermitian Systems,” *Phys. Rev. Lett.* **125**, 126402 (2020).
- [28] Nobuyuki Okuma, Kohei Kawabata, Ken Shiozaki, and Masatoshi Sato, “Topological Origin of Non-Hermitian Skin Effects,” *Phys. Rev. Lett.* **124**, 086801 (2020).
- [29] Zhesen Yang, Kai Zhang, Chen Fang, and Jiangping Hu, “Non-Hermitian Bulk-Boundary Correspondence and Auxiliary Generalized Brillouin Zone Theory,” *Phys. Rev. Lett.* **125**, 226402 (2020).
- [30] Yifei Yi and Zhesen Yang, “Non-hermitian skin modes induced by on-site dissipations and chiral tunneling effect,” *Phys. Rev. Lett.* **125**, 186802 (2020).
- [31] Lei Xiao, Tianshu Deng, Kunkun Wang, Gaoyan Zhu, Zhong Wang, Wei Yi, and Peng Xue, “Non-Hermitian bulk-boundary correspondence in quantum dynamics,” *Nature Physics* **16**, 761–766 (2020).
- [32] Ananya Ghatak, Martin Brandenbourger, Jasper van Wezel, and Corentin Coulais, “Observation of non-Hermitian topology and its bulk-edge correspondence in an active mechanical metamaterial,” *Proceedings of the National Academy of Sciences* **117**, 29561–29568 (2020).
- [33] T. Helbig, T. Hofmann, S. Imhof, M. Abdelghany, T. Kiessling, L. W. Molenkamp, C. H. Lee, A. Szameit, M. Greiter, and R. Thomale, “Generalized bulk-boundary correspondence in non-Hermitian topoelectrical circuits,” *Nature Physics* **16**, 747–750 (2020).
- [34] Linhu Li, Ching Hua Lee, Sen Mu, and Jiangbin Gong, “Critical non-hermitian skin effect,” *Nature Communications* **11**, 5491 (2020).
- [35] Kohei Kawabata, Nobuyuki Okuma, and Masatoshi Sato, “Non-bloch band theory of non-hermitian hamiltonians in the symplectic class,” *Phys. Rev. B* **101**, 195147 (2020).
- [36] Clara C. Wanjura, Matteo Brunelli, and Andreas Nunnenkamp, “Topological framework for directional amplification in driven-dissipative cavity arrays,” *Nature Communications* **11**, 3149 (2020).
- [37] Wen-Tan Xue, Ming-Rui Li, Yu-Min Hu, Fei Song, and Zhong Wang, “Simple formulas of directional amplification from non-bloch band theory,” *Phys. Rev. B* **103**, L241408 (2021).
- [38] Linhu Li, Sen Mu, Ching Hua Lee, and Jiangbin Gong, “Quantized classical response from spectral winding topology,” *Nature Communications* **12**, 5294 (2021).
- [39] Kai Zhang, Zhesen Yang, and Chen Fang, “Universal non-hermitian skin effect in two and higher dimensions,” *Nature Communications* **13**, 2496 (2022).
- [40] Kai Zhang, Chen Fang, and Zhesen Yang, “Dynamical degeneracy splitting and directional invisibility in non-hermitian systems,” *Phys. Rev. Lett.* **131**, 036402 (2023).
- [41] Stefano Longhi, “Self-healing of non-hermitian topological skin modes,” *Phys. Rev. Lett.* **128**, 157601 (2022).
- [42] Yu-Min Hu, Hong-Yi Wang, Zhong Wang, and Fei Song, “Geometric Origin of Non-Bloch PT Symmetry Breaking,” (2022), arXiv:2210.13491.
- [43] Kai Zhang, Zhesen Yang, and Kai Sun, “Edge theory of the non-hermitian skin modes in higher dimensions,” (2024), arXiv:2309.03950 [cond-mat.mes-hall].
- [44] Zeqi Xu, Bo Pang, Kai Zhang, and Zhesen Yang, “Two-dimensional asymptotic generalized brillouin zone theory,” (2024), arXiv:2311.16868 [cond-mat.mes-hall].
- [45] Yi-Cheng Wang, Jihh-Shih You, and H. H. Jen, “A non-hermitian optical atomic mirror,” *Nature Communications* **13**, 4598 (2022).
- [46] Qiuyan Zhou, Jien Wu, Zhenhang Pu, Jiuyang Lu, Xueqin Huang, Weiyin Deng, Manzhu Ke, and Zhengyou Liu, “Observation of geometry-dependent skin effect in non-hermitian phononic crystals with exceptional points,” *Nature Communications* **14**, 4569 (2023).
- [47] Wei Wang, Mengying Hu, Xulong Wang, Guancong Ma,

- and Kun Ding, “Experimental realization of geometry-dependent skin effect in a reciprocal two-dimensional lattice,” *Phys. Rev. Lett.* **131**, 207201 (2023).
- [48] Tuo Wan, Kai Zhang, Junkai Li, Zhesen Yang, and Zhaoju Yang, “Observation of the geometry-dependent skin effect and dynamical degeneracy splitting,” *Science Bulletin* **68**, 2330–2335 (2023).
- [49] Yi Qin, Kai Zhang, and Linhu Li, “Geometry-dependent skin effect and anisotropic bloch oscillations in a non-hermitian optical lattice,” *Phys. Rev. A* **109**, 023317 (2024).
- [50] Entong Zhao, Zhiyuan Wang, Chengdong He, Ting Fung Jeffrey Poon, Ka Kwan Pak, Yu-Jun Liu, Peng Ren, Xiong-Jun Liu, and Gyu-Boong Jo, “Two-dimensional non-hermitian skin effect in an ultracold fermi gas,” (2023), [arXiv:2311.07931](https://arxiv.org/abs/2311.07931).
- [51] Jun Kondo, “Resistance Minimum in Dilute Magnetic Alloys,” *Progress of Theoretical Physics* **32**, 37–49 (1964).
- [52] LUH YU, *Acta Physica Sinica* **21**, 75–91 (1965).
- [53] Hiroyuki Shiba, “Classical spins in superconductors,” *Progress of Theoretical Physics* **40**, 435–451 (1968).
- [54] A. I. Rusinov, “Superconductivity near a paramagnetic impurity,” **9**, 146 (1969).
- [55] Linhu Li, Ching Hua Lee, and Jiangbin Gong, “Impurity induced scale-free localization,” *Communications Physics* **4**, 42 (2021).
- [56] Cui-Xian Guo, Xueliang Wang, Haiping Hu, and Shu Chen, “Accumulation of scale-free localized states induced by local non-hermiticity,” *Phys. Rev. B* **107**, 134121 (2023).
- [57] Naomichi Hatano and David R. Nelson, “Localization transitions in non-hermitian quantum mechanics,” *Phys. Rev. Lett.* **77**, 570–573 (1996).
- [58] Naomichi Hatano and David R. Nelson, “Vortex pinning and non-hermitian quantum mechanics,” *Phys. Rev. B* **56**, 8651–8673 (1997).
- [59] Zixi Fang, Chen Fang, and Kai Zhang, “Point-gap bound states in non-hermitian systems,” *Phys. Rev. B* **108**, 165132 (2023).
- [60] Kohei Kawabata, Masatoshi Sato, and Ken Shiozaki, “Higher-order non-Hermitian skin effect,” *Phys. Rev. B* **102**, 205118 (2020).
- [61] Qiang Wang, Changyan Zhu, Xu Zheng, Haoran Xue, Baile Zhang, and Y. D. Chong, “Continuum of bound states in a non-hermitian model,” *Phys. Rev. Lett.* **130**, 103602 (2023).
- [62] Xiao-Gang Wen, *Quantum field theory of many-body systems: From the origin of sound to an origin of light and electrons* (OUP Oxford, 2004).
- [63] When $|b|^2 \leq \frac{\sin(\arg a)^2}{\sin(\arg a - \arg b) \sin(\arg b)}$, $k_x k_y$ term can always be eliminated through a suitable rotation.
- [64] See Supplementary Material for more details.
- [65] $\sigma_{\text{OBC}} = \sigma_{\text{PBC}}$ in the system with GDSE.
- [66] Hong-Yi Wang, Fei Song, and Zhong Wang, “Amoeba formulation of the non-hermitian skin effect in higher dimensions,” *arXiv preprint arXiv:2212.11743* (2022).
- [67] Mikael Passare and August Tsikh, “Amoebas: their spines and their contours,” *Contemporary Mathematics* **377**, 275–288 (2005).
- [68] I.M. Gelfand, M. Kapranov, and A. Zelevinsky, *Discriminants, Resultants, and Multidimensional Determinants* (Birkhäuser Boston, 2013).
- [69] Vitaly A. Krasikov, “A survey on computational aspects of polynomial amoebas,” *Mathematics in Computer Science* **17**, 16 (2023).

Supplementary Material for “Point-Gap Bound States in Non-Hermitian Systems”

CONTENTS

S-1. Proof of relation between the bound state and contour of amoeba	8
A. Formation of Geometry of Bound State	8
B. Proof of the relation	9
C. Some technical details concerning deforming integration contour	9
S-2. discussion on weak impurity limit	10
A. GDSE Amoeba at weak impurity	10
B. Equal amplitude of wave function	11
C. Effect of weak non-Hermiticity	12
D. relationship of the argument of bound state energy and impurity	12
S-3. Local Density of States	12
S-4. Discussion on strong impurity case	13
References	14

S-1. PROOF OF RELATION BETWEEN THE BOUND STATE AND CONTOUR OF AMOEBA

In this section, we shall present our theory on geometry of bound state with more technical details. First, we shall explicitly formulate the wavefunction following the method in the maintext. Then we move on to the proof for the relationship between geometry of wavefunction and amoeba’s contour, i.e., the inverse of localization length at a given direction is determined by the point in the amoeba whose normal line is parallel to that direction. After that, some technical details concerning the deformation of the integration contour are discussed.

A. Formation of Geometry of Bound State

We begin with the generalization of Green function method. The wavefunction is determined by

$$\begin{aligned}\psi_E(x, y) &= \lambda\psi_E(0, 0)G_0(E; x, y) \\ &= \lambda\psi_E(0) \oint_{z_x, z_y \in \mathbb{S}^1} \frac{dz_x dz_y}{(2\pi i)^2} \frac{z_x^x z_y^y}{z_x z_y (E - \mathcal{H}_0(z_x, z_y))}\end{aligned}\quad (\text{S1})$$

where $\mathcal{H}_0(z_x \equiv e^{ik_x}, z_y \equiv e^{ik_y}) = \sum_{l=-m, s=-n}^{l=M, s=N} t_{s,l} z_x^s z_y^l$ is the Hamiltonian in bivariate Laurant polynomial form defined in the main text. Integrate with respect to z_y using residue theorem (here we assume $x, y > 0$, so we choose residue inside the unit circle),

$$\begin{aligned}\psi_E(x, y) &= \lambda\psi_E(0) \oint_{z_x \in \mathbb{S}^1} \frac{dz_x}{2\pi i} \sum_{|z_y| < 1} R(E, z_y(z_x)) \times \\ &\quad e^{\ln z_x(x+m-1) + \ln z_y(y+n-1)}\end{aligned}\quad (\text{S2})$$

Here $R(E, z_{y,i}) = -1/t_{M,N} \prod_{j(\neq i)=1}^{N+n} (z_{y,j} - z_{y,i})$ is the residue of the function $z_x^m z_y^n (E - \mathcal{H}_0)$ at pole $z_{y,i}$, and the pole $z_{y,i}(z_x)$ is actually a function of z_x , i.e., $z_{y,i}(z_x)$ are roots of $E - \mathcal{H}_0(z_x, z_y) = 0$ for z_y given z_x . Since we only care about the asymptotic behavior at infinity, we can assume $x + m - 1 \approx x$, $y + n - 1 \approx y$ and evaluate above equation with saddle point approximation,

$$\psi_E(x, y) = \lambda\psi_E(0) \sum_{\kappa_x, \kappa_y} R_{ES}(e^{i\kappa_x}, e^{i\kappa_y}) e^{i\kappa_x x + i\kappa_y y}\quad (\text{S3})$$

where κ_x, κ_y is given by

$$\frac{x}{z_x} + y \partial_{z_x} \ln z_y(z_x) = 0 \quad (\text{S4})$$

Denote $f(z_x, z_y) := E - \mathcal{H}_0(z_x, z_y)$, and replace $\partial_{z_x} \ln z_y(z_x)$ in above equation with implicit function theorem, one can find

$$\frac{x}{z_x} - \frac{y}{z_y} \frac{\partial_{z_x} f}{\partial_{z_y} f} = 0 \quad (\text{S5})$$

In next subsection, we shall see that this result is in accordance with the definition of amoeba's contour.

B. Proof of the relation

In this subsection, we shall prove that the saddle point determining the localization length of the bound state is given by points in the contour of amoeba.

We shall begin with an introduction to the theory of amoeba contour [1–3]. Consider a bivariate Laurent form polynomial $f(z_x, z_y) = \sum_{t,s} a_{t,s} z_x^t z_y^s$, the contour of its amoeba is defined as

$$\mathcal{C}_f = \{(\log|z_x|, \log|z_y|) \in \mathbb{R}^2 | f(z_x, z_y) = 0, k z_x \partial_{z_x} f - z_y \partial_{z_y} f = 0, k \in \mathbb{R} \cup \{\pm\infty\}\} \quad (\text{S6})$$

Here k is a real parameter that encodes the slope of the normal line to the contour of the amoeba. The boundary of amoeba is a subset of its contour \mathcal{C}_f .

One can intuitively understand this definition by following considerations. Let a point $(z_{x0}, z_{y0}) \equiv (e^{\mu_{x0} + ik_{x0}}, e^{\mu_{y0} + ik_{y0}})$ sit at the boundary of the amoeba, then a neighbor point $(e^{\mu_{x0} + ik_{x0} + \delta\mu_x + i\delta k_x}, e^{\mu_{y0} + ik_{y0} + \delta\mu_y + i\delta k_y})$ is mapped to

$$f(e^{\mu_{x0} + ik_{x0} + \delta\mu_x + i\delta k_x}, e^{\mu_{y0} + ik_{y0} + \delta\mu_y + i\delta k_y}) = f(z_{x0}, z_{y0}) + (\delta\mu_x + i\delta k_x) z_x \partial_{z_x} f + (\delta\mu_y + i\delta k_y) z_y \partial_{z_y} f + \mathcal{O}(\delta\mu^2, \delta k^2) \quad (\text{S7})$$

Giving a pair $(\delta\mu_x, \delta\mu_y)$ and treating $(\delta k_x, \delta k_y)$ as variables, one can always find a solution for $(\delta k_x, \delta k_y)$ such that $(\delta\mu_x + i\delta k_x) z_x \partial_{z_x} f + (\delta\mu_y + i\delta k_y) z_y \partial_{z_y} f = 0$ if this equation is not degenerate. In other words, to find a neighbor point not in the amoeba, $(z_x \partial_{z_x} f, z_y \partial_{z_y} f)$ must be \mathbb{R} -dependent, which gives the second relation in Eq. S6.

In Eq. S6, treating f as giving an implicit function $z_x(z_y)$, then one get

$$\frac{z_y}{z_x} \frac{dz_x}{dz_y} = -k = \frac{d \ln z_x}{d \ln z_y} = \frac{1}{2} \left(\frac{\partial \mu_x}{\partial \mu_y} - i \frac{\partial \mu_x}{\partial k_y} \right) + i \frac{1}{2} \left(\frac{\partial k_x}{\partial \mu_y} - i \frac{\partial k_x}{\partial k_y} \right) \quad (\text{S8})$$

A few remarks shall be noted. First, the second term in the last equation naturally equals the first term by holomorphicity. Second, taking the imaginary part of the last equation above, one immediately gets $\frac{\partial \mu_x}{\partial k_y} = 0$. Taking the real part, one gets $k \frac{\partial \mu_y}{\partial \mu_x} = -1$, which implies k is the slope of the normal line to the contour of the amoeba as we mentioned above.

C. Some technical details concerning deforming integration contour

In this subsection, we provide some technical details concerning the deformation of the integration contour in the calculation of the localization length.

Note that the statement that the localization length of the bound state is given by the saddle point of the integral is valid only when we can deform the contour of the integral to the saddle point without touching the poles of the integrand. In the following, we shall show that this is indeed the case since the poles are always discrete points in the complex plane for z_y .

Note that after integration of z_x , we get (some constants are dropped for simplicity)

$$\int_{z_y \in S^1} dz_y \sum_i \frac{z_{x,i}^s(z_y) z_y^t}{\prod_{j \neq i} (z_{x,i}(z_y) - z_{x,j}(z_y))} \quad (\text{S9})$$

As a function of z_y , $z_{x,i}(z_y)$ is analytical in the complex plane but for some discrete points. Indeed, $f(z_x, z_y) = E - \mathcal{H}(z_x, z_y) = 0$ gives this implicit function and $\partial_{z_y} z_x = -\partial_{z_y} f / \partial_{z_x} f$ is not differentiable only when $\partial_{z_x} f = 0$. Jointing this constraint with $E - \mathcal{H}(z_x, z_y) = 0$, one can only get finitely many points in the complex plane.

The same argument holds for the numerator, since $z_{x,i} - z_{x,j} = 0$ pose the other constraint and thus only leads to finite many poles.

S-2. DISCUSSION ON WEAK IMPURITY LIMIT

In this section, we shall discuss the weak impurity limit for GDSE case in more detail. We shall first perturbatively solve the contour of amoeba for such case and then we can get the condition for the argument of energy at which irregularity appears. After that, we will describe what can be expected from the bound state when one imposes a weak non-Hermiticity to a Hermitian system and show the relationship between the argument of bound state energy and that of impurity.

A. GDSE Amoeba at weak impurity

As shown in the main text, at weak impurity, the bound state takes energy near the Bloch Saddle Point and after a transforming of variables, we only need to consider the model $-2 \cos k_x - 2e^{i\theta} \cos k_y$, where a factor of 2 is added for the sake of simplicity. We point out here that this model has inversion symmetry $k_x \rightarrow -k_x, k_y \rightarrow -k_y$, thus the amoeba and its contour should also be symmetric with respect to inversion on x and y axis. Expand the Hamiltonian near the Bloch Saddle Point $(k_x, k_y) = (0, 0)$,

$$h_0(\kappa_x, \kappa_y) = -2 - 2e^{i\theta} + (k_x - i\mu_x)^2 + e^{i\theta}(k_y - i\mu_y)^2 \quad (\text{S10})$$

with complex momentum $\kappa_{x(y)} = k_{x(y)} - i\mu_{x(y)}$. By substituting this Hamiltonian into Equations 9 and 10 in the main text, we obtain equations for two complex number domains, that is, four equations for the real number domain.

$$\text{Re}(\delta E - (k_x - i\mu_x)^2 - e^{i\theta}(k_y - i\mu_y)^2) = 0 \quad (\text{S11})$$

$$\text{Im}(\delta E - (k_x - i\mu_x)^2 - e^{i\theta}(k_y - i\mu_y)^2) = 0 \quad (\text{S12})$$

$$\text{Re}(k(k_x - i\mu_x) - e^{i\theta}(k_y - i\mu_y)) = 0 \quad (\text{S13})$$

$$\text{Im}(k(k_x - i\mu_x) - e^{i\theta}(k_y - i\mu_y)) = 0 \quad (\text{S14})$$

where $\delta E = E - (-2 - 2e^{i\theta})$. We can eliminate the variables k_x and k_y by solving Eq. S13 and Eq. S14, and substitute k_x and k_y into Eq. S11 and Eq. S12. And because Eq. S11 and Eq. S12 have the same k for each μ_x, μ_y . Then we can use the resultant to find the final result $f_{\delta E}(\mu_x, \mu_y) = 0$. $f_{\delta E}(\mu_x, \mu_y) = 0$ is a algebraic curve with parameters in $(|\delta E|, \arg(\delta E))$. Further notice $f_{\delta E}(\mu_x, \mu_y)$ is homogeneous with respect to $(\mu_x, \mu_y, |\delta E|^{\frac{1}{2}})$ (which originates from Eq. S10) and one can perform the variable change $(\mu_x, \mu_y) \rightarrow (\mu'_x |\delta E|^{\frac{1}{2}}, \mu'_y |\delta E|^{\frac{1}{2}})$ to eliminate $|\delta E|$. Here we list the result (denote $\alpha := \arg(\delta E)$) and we dropped superscript for simplicity)

$$\begin{aligned} f(\mu_x, \mu_y) &= R(f_1(\mu_x, \mu_y, k), f_2(\mu_x, \mu_y, k), k) \quad (\text{S15}) \\ f_1(\mu_x, \mu_y, k) &= -k^2 \cos(\alpha) + k^2 \csc^2(\theta) \mu_x^2 (\cos(2\theta) + k^2 \cos(\theta)) \\ &\quad - 2k \csc^2(\theta) \mu_x \mu_y (\cos(\theta) + k^2) + \csc^2(\theta) \mu_y^2 (k^2 \cos(\theta) + 1) \\ f_2(\mu_x, \mu_y, k) &= -k \csc(\theta) \mu_x^2 (2 \cos(\theta) + k^2) + k (\sin(\alpha) + \csc(\theta) \mu_y^2) + 2 \csc(\theta) \mu_x \mu_y \end{aligned}$$

Here $f(\mu_x, \mu_y)$ is the equation of amoeba's contour, and $f_1(\mu_x, \mu_y, k)$ and $f_2(\mu_x, \mu_y, k)$ are deformations of Eq. S11 and Eq. S12, and $R(f(x), g(x), x)$ is the resultant of the polynomials $f(x)$ and $g(x)$ with respect to the variable x. Fig S1 plots $f(\mu_x, \mu_y)$ for different $\arg(\delta E)$ with fixed $\theta = \frac{\pi}{3}$. Only when δE takes value outside spectrum, i.e. $\arg(\delta E) \notin (0, \theta)$, can a central hole be found. As described in the main text, one may also observe that when $\arg(\delta E) \in (\theta, 2\theta)$ (symmetrically, $\arg(\delta E) \in (0, -\theta)$), irregularity takes place at $x(y)$ axis. In the following we shall make this observation valid.

Let's take irregularity at x axis as an example and y axis can be treated similarly. Solve the equation $f(\mu_x, 0) = 0$,

$$\begin{aligned} \mu_{x,1} &= \sqrt{\frac{1 - \cos(\arg \delta E)}{2}}, \mu_{x,2} = \sqrt{\frac{-1 - \cos(\arg(\delta E))}{2}}, \mu_{x,3,4} = \sqrt{\frac{\sin(\theta) \sin(\arg(\delta E) - \theta)}{2}} \\ \mu_{x,i} &= -\mu_{x,i-4}, i = 5, 6, 7, 8 \end{aligned} \quad (\text{S16})$$

Here we only need to deal with the first four roots since the remaining is just the inverse. Note that $\mu_{x,2}$ is always imaginary and $\mu_{x,1}$ is always real and regular. One can also check that $\mu_{x,3,4}$ appears as an irregular point, since it's also a solution for $\partial_{\mu_x} f = 0, \partial_{\mu_y} f = 0$. Thus, to make $\mu_{x,3,4}$ real, one need $\sin(\arg(\delta E) - \theta) > 0$ (we can always assume

$\theta \in (0, \pi)$). Then, recall that to make such an irregular point not isolated in the real plane, its Hessian matrix of second derivatives should have both positive and negative eigenvalues, and this gives the other side of the constraint. The Hessian matrix for $\mu_{x,3,4}$ reads as $diag(64 \sin(\theta) \sin(\theta - \arg(\delta E)) \sin^2(2\theta - \arg(\delta E)), 64 \sin(\theta) \sin^3(2\theta - \arg(\delta E))$. Take both constraints and the proposition is proved.

B. Equal amplitude of wave function

Because amoeba's contour determines the localization length (determined by equation $x\mu_x + y\mu_y = 1$) of the wave function along a certain direction y/x , it is able to get the corresponding curves of the localization length of the wave function along different directions through amoeba's contour Eq S15, which is also the curve of the equal amplitude of the wave function.

$$2(\sin(\alpha)x^2 + \sin(\alpha - \theta)y^2)^2 - 8(\cos(\alpha)x^2 + \cos(\alpha - \theta)y^2 + 1) = 0 \quad (\text{S17})$$

This curve is deemed concave if it exhibits negative and positive curvature along its path, so the transition point between a concave curve and a convex curve is the point at which zero curvature first appears in the path. Using the Hessian matrix to calculate the curvature of the curve, we can find that zero curvature exists in the region with $0 < |\alpha - \theta| < \theta$.

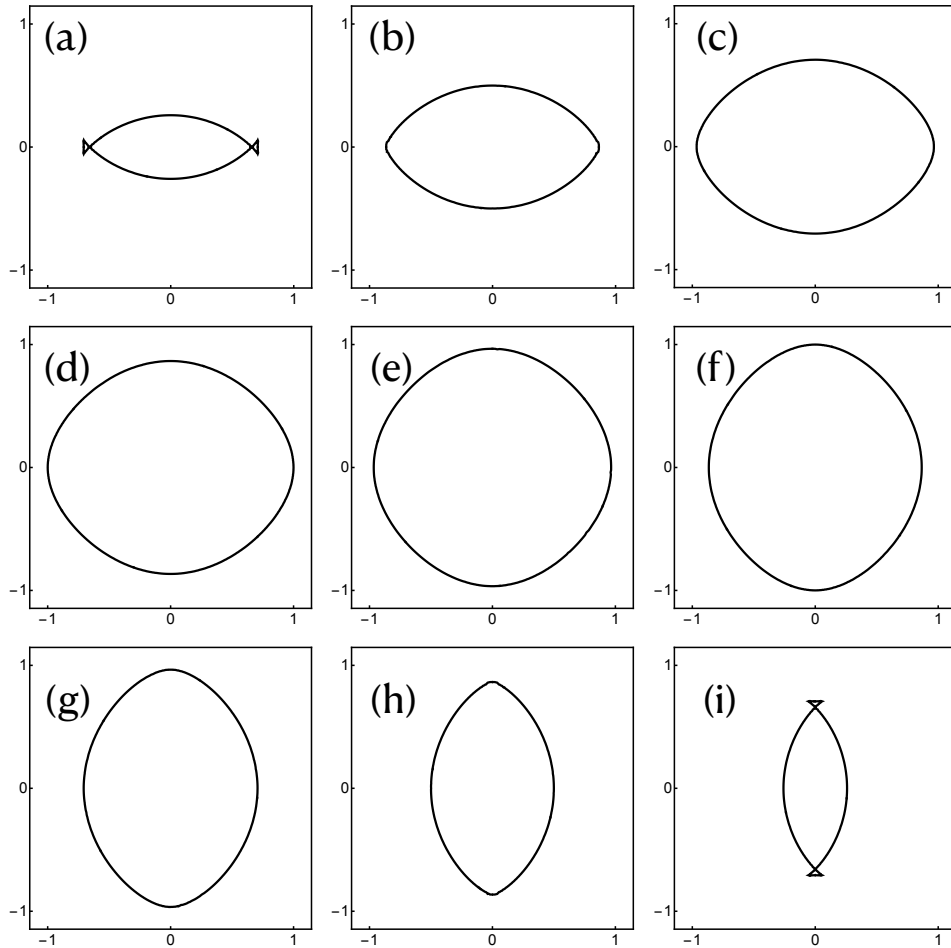


FIG. S1. $f(\mu_x, \mu_y) = 0$ in Eq.S15 for different α . Fix $\theta = \frac{\pi}{3}$ (a) $\alpha = \frac{\pi}{2}$; (b) $\alpha = \frac{2\pi}{3}$; (c) $\alpha = \frac{5\pi}{6}$; (d) $\alpha = \pi$; (e) $\alpha = \frac{7\pi}{6}$; (f) $\alpha = \frac{4\pi}{3}$; (g) $\alpha = \frac{3\pi}{2}$; (h) $\alpha = \frac{5\pi}{3}$; (i) $\alpha = \frac{11\pi}{6}$;

C. Effect of weak non-Hermiticity

Let's first recast some facts on wavefunction in the Hermitian lattice case in the language of amoeba. In Eq. S15, let $\theta = 0$ and one get

$$f_{\theta=0}(\mu_x, \mu_y) = g(\mu_x^2 + \mu_y^2) \quad (\text{S18})$$

The precise form of the function g is not important. What matters here is that $\mu_x^2 + \mu_y^2$ appears in the function as a whole due to symmetry, which we can also get from eq.S10. This implies that the contour should be a circle, whose radius can be read from eq.S16 as $\mu_{x,1}$. Thus, the wavefunction here is isotropic with localization length $\frac{1}{|\delta E|^{\frac{1}{2}} \mu_{x,1}(\arg(\delta E))}$.

A few corollaries are ready in hand. First, comparing with the a real δE , a complex one with same strength tends to suppress the localization of wavefunction. Second, when x and y are not symmetric, i.e., the hoppings are different, the contour of amoeba shall take the form of an ellipse and so will the geometry of wavefunction. One may also note that the mix term μ_x, μ_y shall rotate the orientation of this ellipse.

Next, we fix the bound state energy real ($\arg \delta E = \pi$) and show the result when one poses the non-Hermiticity to the lattice. In eq.S15, fix a direction by defining $\mu_y = k\mu_x, r^2 = \mu_x^2 + \mu_y^2$ and treat $f(\frac{r}{\sqrt{1+k^2}}, \frac{kr}{\sqrt{1+k^2}})$ as an implicit function of $r(\theta)$ with parameters of k , allowing one to expand it at $\theta = 0$

$$r(\theta) = -\frac{1}{8}k^2\left(\frac{1}{1+k^2}\right)^2(2+k^2)\theta^2 + O(\theta^4) \quad (\text{S19})$$

Note that the odd powers of terms naturally vanish since it's an even function. The negativity of the coefficient of the second order implies that in this case non-Hermiticity also suppresses the localization of the bound state. Further notice $r''(\theta)|_{\theta=0}$ as a function of k is monotone in $(0, \infty)$ and $(-\infty, 0)$ and vanishes at minimal $k = 0$, so such suppression is not isotropic and do not influence localization at x axis, a fact which can also be retained from Eq. S16 and understood intuitively since non-Hermiticity is only imposed to y axis.

D. relationship of the argument of bound state energy and impurity

In the main text, we established the relationship between bound state energy and impurity near bloch saddle point via evaluating the integral with model $\cos k_x + a \cos k_y + b \sin k_x$, i.e.

$$\begin{aligned} \lambda^{-1} &= \frac{1}{4\pi^2} \int_{BZ} \frac{dk_x dk_y}{1 + 1a + \delta E - \cos k_x - a \cos k_y - b \sin k_x} \\ &= \frac{2K\left(\frac{4a\sqrt{1+b^2}}{(\delta E+1+\sqrt{1+b^2})(\delta E+2a+1-\sqrt{1+b^2})}\right)}{\pi\sqrt{(\delta E+1+\sqrt{1+b^2})(\delta E+2a+1-\sqrt{1+b^2})}} \end{aligned} \quad (\text{S20})$$

Note that $K(x)$, the Complete elliptic integral of the first kind, has asymptotic expansion near 1 as $K(1-x) \sim -\frac{\ln(x)}{2}$, and one can get

$$\delta E \sim \frac{4ae^{-\frac{\sqrt{a}\pi}{\lambda}}}{1+a} \quad (\text{S21})$$

Thus, the argument of bound state energy is linear with respect to the argument of impurity, i.e.

$$\arg(\delta E) \sim \arg\left(\frac{a}{1+a}\right) - \left|\frac{\sqrt{a}}{\lambda}\right| \left(\frac{1}{2}\arg(a) - \arg(\lambda)\right) \quad (\text{S22})$$

S-3. LOCAL DENSITY OF STATES

In this section, we will illustrate how the concavity and convexity of the wave function is reflected in LDOS by calculating LDOS. We consider a non-Hermitian system H_0 with an impurity $V = \lambda|0,0\rangle\langle 0,0|$ at the origin. Through

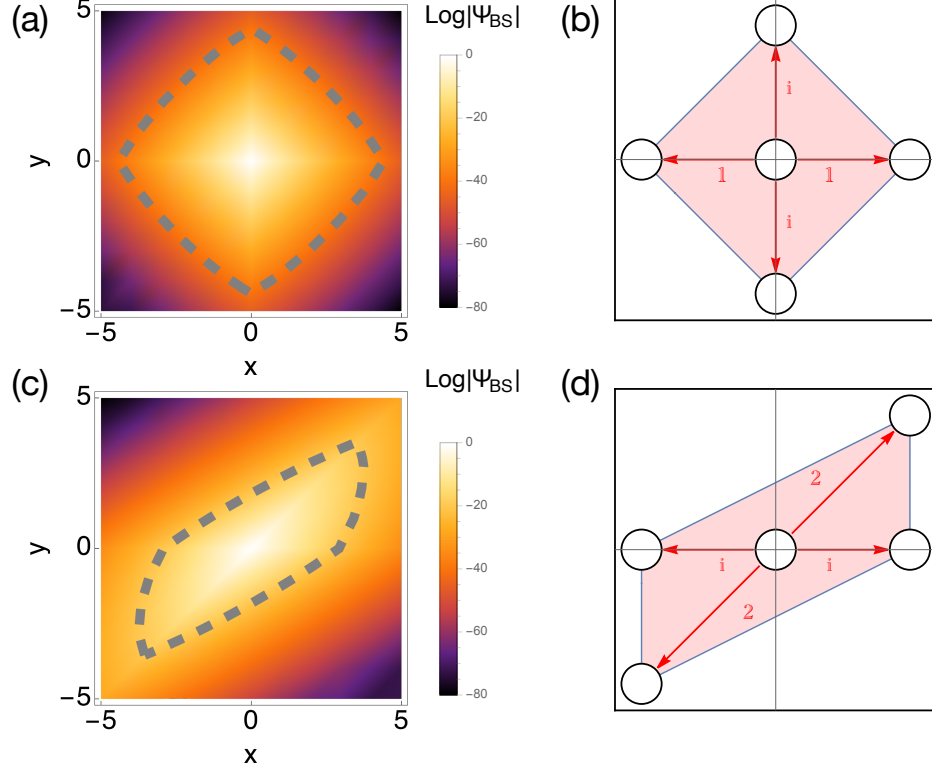


FIG. S2. Parameters $\{t_{1,1}, t_{1,0}, t_{-1,0}, t_{0,-1}, t_{0,1}, t_{-1,-1}\}$ for Hamiltonian are chosen to be $\{0, 1, 1, i, i, 0\}$ in (a) and (b), and $\{2, i, i, 0, 0, 2\}$ in (c) and (d). Panels (a) and (c) depict the shape of the bound state, while panels (b) and (d) show the corresponding Newton polytope. The results are obtained from simulations performed on a 30×30 lattice, with data extracted from the central 11×11 sites with the impurity strength set to $\lambda = 50$.

perturbation theory, we can know that when impurities are added, the Green's function of the system can be calculated as,

$$G(\omega; x, y) = g_0(\omega) + \frac{G_0(\omega; x, y)G_0(\omega; -x, -y)}{1/\lambda - g_0(\omega)} \quad (\text{S23})$$

here $G(\omega; x, y) = \langle x, y | 1/(\omega - H_0 - V) | x, y \rangle$ represents the perturbed Green's function, $G_0(\omega; x, y) = \langle x, y | 1/(\omega - H_0) | 0, 0 \rangle$ represents the unperturbed Green's function with its entity at origin denoted as $g_0(\omega) = G_0(\omega; 0, 0)$.

From Eq. 3 in the text, we can know that $G_0(\omega; x, y)$ is proportional to the wave function of the bound state, and based on the previous discussion, we know that under the limit of weak impurity, the amoeba contour that determines the wave function has inversion symmetry about the origin. Therefore, our wave function should have inversion symmetry, so that our Green's function is proportional to the square of the wave function. As a result, LDOS will inherit the concavity and convexity of the wave function.

S-4. DISCUSSION ON STRONG IMPURITY CASE

As the impurity strength increases, the shape of the bound state wave function progressively approximates a polygon and ultimately can be represented by a polytope known as the Newton Polytope, which is determined by the Bloch Hamiltonian. The Newton Polytope of a polynomial is defined as the convex hull of the set of exponent vectors of monomials within it. Physically, the Newton Polytope is analogous to the convex hull of the hopping graph, which represents all the hopping terms in the Hamiltonian, as illustrated in Fig S2(b) and (d).

As the impurity strength increases, the central hole of the amoeba expands and retreats to its spine, which is a dual representation of the system's Newton Polytope. Since the shape of the wave function is dictated by its localization

length—a dual of the amoeba’s contour, which encompasses the central hole, the wave function’s shape resembles that of the Newton Polytope.

In Fig. S2, we present the results for two examples of Hamiltonians. The first model incorporates the nearest hopping term, leading to a diamond-shaped Newton Polytope as illustrated in Fig. S2(b). The corresponding wavefunction is plotted in Fig. S2(a), exhibiting a diamond-like form. Conversely, the second model features a parallelogram-shaped Newton Polytope shown in Fig. S2(d), accompanied by its parallelogram-like wave function depicted in Fig. S2(c).

-
- [1] Passare, M. & Tsikh, A. Amoebas: their spines and their contours. *Contemporary Mathematics* **377**, 275–288 (2005).
 - [2] Gelfand, I., Kapranov, M. & Zelevinsky, A. *Discriminants, Resultants, and Multidimensional Determinants* (Birkhäuser Boston, 2013). URL <https://books.google.nl/books?id=PC4AswEACAAJ>.
 - [3] Krasikov, V. A. A survey on computational aspects of polynomial amoebas. *Mathematics in Computer Science* **17**, 16 (2023). URL <https://doi.org/10.1007/s11786-023-00570-x>.